Hindawi
Adsorption Science & Technology
Volume 2022, Article ID 4282485, 11 pages
https://doi.org/10.1155/2022/4282485

Research Article

Bunch of Grape-Like Shape PANI/Ag_2O/Ag Nanocomposite Photocatalyst for Hydrogen Generation from Wastewater

N. M. A. Hadia,[1,2] Ali Hajjiah,[3] Asmaa M. Elsayed,[4] S. H. Mohamed,[5,6] Mansoor Alruqi,[7] Mohamed Shaban,[4,5] Fatimah Mohammed Alzahrani,[8] Ahmed Adel A. Abdelazeez,[9] and Mohamed Rabia[4,10]

[1]*Physics Department, College of Science, Jouf University, Al-Jouf, Sakaka, P.O. Box 2014, Saudi Arabia*
[2]*Basic Sciences Research Unit, Jouf University, Sakaka, P.O. Box 2014, Saudi Arabia*
[3]*Electrical Engineering Department, College of Engineering and Petroleum, Kuwait University, Safat 13113, Kuwait*
[4]*Nanophotonics and Applications Lab, Physics Department, Faculty of Science, Beni-Suef University, Beni-Suef 62514, Egypt*
[5]*Physics Department, Faculty of Science, Islamic University of Madinah, P.O. Box 170, Madinah 42351, Saudi Arabia*
[6]*Physics Department, Faculty of Science, Sohag University, 82524 Sohag, Egypt*
[7]*Department of Mechanical Engineering, College of Engineering, Shaqra University, Al Riyadh 11911, Saudi Arabia*
[8]*Chemistry Department, College of Science, Princess Nourah Bint Abdulrahman University, Riyadh 11671, Saudi Arabia*
[9]*Nanoscale Science, Chemistry Department, University of North Carolina at Charlotte, Charlotte, North Carolina 28223, USA*
[10]*Nanomaterials Science Research Laboratory, Chemistry Department, Faculty of Science, Beni-Suef University, Beni-Suef 62514, Egypt*

Correspondence should be addressed to Ali Hajjiah; ali.hajjiah@ku.edu.kw
and Mohamed Rabia; mohamedchem@science.bsu.edu.eg

Received 5 April 2022; Accepted 10 May 2022; Published 29 May 2022

Academic Editor: Hassan M. Hassan

Polyaniline (PANI) and PANI/Ag_2O/Ag composites I and II were prepared under different $AgNO_3$ oxidant concentrations using the oxidative photopolymerization method. The chemical structure and optical, electrical, and morphological properties were determined for the prepared nanocomposite. The PANI/Ag_2O/Ag composite II has the optimum optical properties, in which the bandgaps of PANI, composite I, and composite II are 3.02, 1.71, and 1.68 eV, respectively, with the morphology of a bunch of grape-like shapes with average particles sizes of 25 nm. Under the optimum optical properties, glass/PANI/Ag_2O/Ag composite II electrode is used for hydrogen generation from sewage water. The measurements are carried out from a three-electrode cell under a xenon lamp. The effects of light wavelengths and temperature on the produced current density (J_{ph}) are mentioned. Under the applied voltage (at 30°C), the current density values (J_{ph}) increase from 0.003 to 0.012 mA.cm^{-2} in dark and light, respectively. While increasing the temperature, J_{ph} values increase to 0.032 mAcm^{-2} at 60°C. The thermodynamic parameters are calculated, in which the activation energy (E_a), enthalpy ($\Delta H*$), and entropy ($\Delta S*$) values are 27.1 kJ·mol^{-1}, 24.5 J mol^{-1}, and 140.5 J K^{-1} mol^{-1}, respectively. Finally, a simple mechanism for the produced hydrogen generation rate is mentioned. The prepared electrode is a very cheap (1$ for 12 * 12 cm^2) electrode.

1. Introduction

Global energy demand is increasing rapidly, because of population and economic growth, especially in emerging market economies. While accompanied by greater prosperity, rising demand creates new challenges. Energy security concerns can emerge as more consumers require ever more energy resources. And higher consumption of fossil fuels leads to higher greenhouse gas emissions, particularly carbon dioxide (CO_2), which contribute to global warming. Moreover, there

are additional gases such as SOx and NOx that have fatal and hazardous effects on plants, animals, humans, and the environment [1–4]. At the same time, the number of people without access to electricity remains unacceptably high.

Many studies were carried out for providing other renewable energy sources such as solar energy, geothermal heat, biomass, and wind. Solar energy is a promising renewable energy source with its applications in photoelectrochemical water splitting reactions [5–8]. This reaction is based on the electron generation under light irradiation, in which the outer energy levels split under this irradiation and cause the hole-electron generation. Both electrons and holes share in the water splitting reaction through the motivation of the H_2O molecule for converting to hydroxyl radicals [9, 10]. The water splitting reaction produces hydrogen gas, which is a promising fuel for the combustion process without any contamination or carbon residue. In addition, this gas has a high energy capacity that can be used in factories, cars, airplanes, and spacecraft.

The gas generation from water splitting is carried out using a semiconductor oxide material such as Cu_2O, ZnO, WO_3, TiO_2, and Fe_2O_3 [11–16]. Metal sulfides such as PbS and CdS can be used as photocatalytic materials for the water splitting reaction and hydrogen generation, but with low efficiency and with some corrosion limitations [17–19]. Sometimes, the carbon materials such as g-C_3N_4 and carbon nanotube have the photocatalytic behavior for water splitting reaction.

Conducting polymers such as PANI and its derivatives are considered promising materials for photocatalytic water splitting reactions. These polymers have great advantages represented in the high surface area, stability, safety, and reproducibility; moreover, they have commercial advantages of low cost and easy preparation [20–22]. The photocatalytic behavior of these polymers increases with increasing the surface area through the nanoscale or polymer composite preparations.

Among great materials as the noble metals such as Pt, Au, and Ag [17, 18, 23], these metals have a plasmonic property that captures the photons and generates electrons on their surface, in which an oscillation process occurs for these electrons. The generated energy is transferred to the neighbor semiconductor materials for more electron generations that finally reach the water molecules for a splitting reaction.

There were previous studies for using polymers as photocatalytic materials. Xiao et al. [24] studied WS_2/poly(3,4-ethylene dioxythiophene)/Au photoelectrode for H_2 generation from H_2O. Mobidane et al. [25] synthesized a poly(3-aminobenzoic acid)/organic framework for hydrogen generation from H_2SO_4 solution. Thimsen et al. [26] studied the role of noble metals on Fe_2O_3 for hydrogen generation from NaOH solution. Moreover, Ghosh et al. [27] studied the contaminations decompositions using the thiophene polymer compounds using the photocatalytic behavior of this polymer. Also, Yin and Zheng [28] use the polymer (poly (diphenyl butadiyne)) for the removal of pollution from fiber materials.

Although the previous studies try to provide a renewable energy source instead of fossil fuels, there are still many limitations represented in the small J_{ph} values related to the small hydrogen moles. Also, the previous studies usually use sacrificing agents such as NaOH, H_2SO_4, Na_2SO_4, and Na_2S in water splitting reactions [23–25]. Moreover, the water source was fresh dist. water. The problem of using high-technology devices in the preparation process still presents with high economic costs such as using a pulsed laser, atomic layer deposition, and RF sputtering techniques [29–32].

This work is promising for providing H_2 gas as a renewable energy source from sewage water without using any freshwater or sacrificing agent. Moreover, the photoelectrode has high stability and reproducibility, in addition to its very low cost. The produced H_2 moles are greater in comparison with the previous studies.

This work studies the preparation of PANI and PANI/Ag_2O-Ag composites I and II for hydrogen generation from sewage water. Composite II is applied as a photoelectrode for hydrogen generation through the three-electrode cell. The effects of dark/light, light wavelengths, and temperature on the produced J_{ph} values were studied.

2. Experimental Part

2.1. Materials. Aniline and $AgNO_3$ were purchased from Rankem (India) and Winlab (UK) companies, respectively. DMSO was obtained from Sigma-Aldrich, USA. NaCl, $Na_2S_2O_3$, CH_3COOH, and NaOH were purchased from El-Nasr Chemicals Company, Egypt.

2.2. Preparation of PANI and PANI/Ag_2O/Ag Composites. PANI was prepared by an in situ oxidative polymerization method, in which 0.1 M aniline was dissolved in acetic acid; in the same manner, 0.15 M $(NH_4)_2S_2O_8$ was dissolved. Then, a sudden addition was carried out, in which the green precipitate indicates the formation of the PANI. This powder is then washed well and dried at 60°C.

PANI/Ag_2O/Ag composites are prepared by the oxidative photopolymerization process, in which $AgNO_3$ is used as an oxidant. Two composites are prepared dependent on the $AgNO_3$ concentrations: composite I and composite II are prepared by using 0.1 and 0.2 M $AgNO_3$, respectively. An artificial light lamp is used (400 W) as the light radiation source. This radiation enhances the oxidation power of $AgNO_3$. The gray-green precipitation indicates the formation of the precipitate.

2.3. Electrode for Hydrogen Generation. PANI/Ag_2O/Ag II composite electrode is prepared for hydrogen generation. The preparation was carried out through oxidative photopolymerization on a glass electrode as shown in Figure 1(a). The prepared glass/PANI/Ag_2O/Ag II electrode is washed well using the dist. water and dried at 60°C. This electrode is used as a working electrode, while graphite and calomel electrodes are used as counter and reference electrodes, respectively. The measurements are carried out from sewage water (chemical composition is mentioned in Table 1). The system of measurements is mentioned in Figure 1(b), in

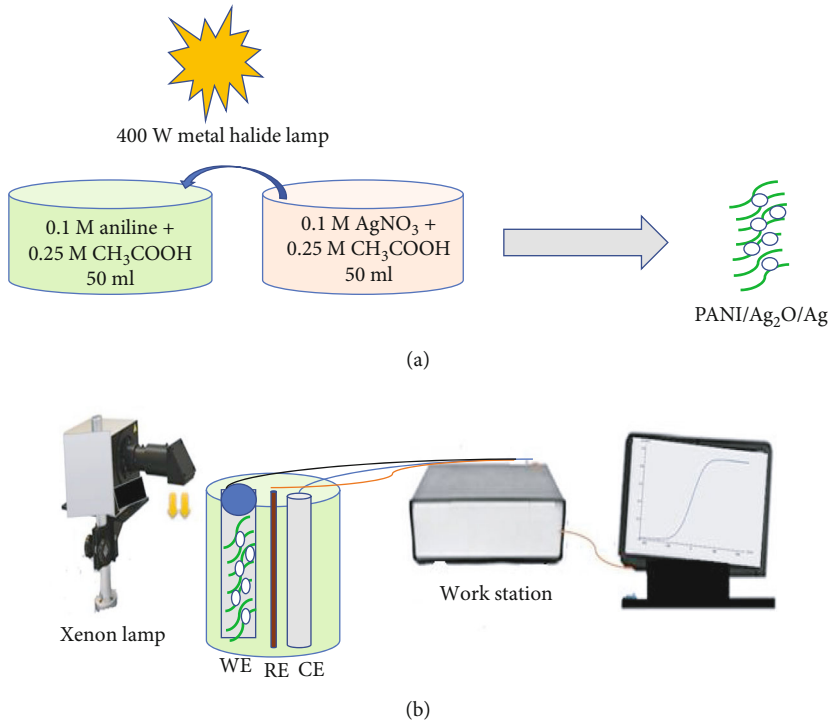

Figure 1: (a) The preparation of the PANI/Ag_2O/Ag composite and (b) the electrochemical system of hydrogen generation through an electrochemical PowerStation and a xenon lamp.

Table 1: The chemical composition of the sewage water-electrolyte for H_2 production.

Material or element	Concentration (mg/L)
Phenols	0.015
F^-	1.0
Al^{3+}	3.0
NH_3	5.0
Hg^{2+}	0.005
Pb^{2+}	0.5
$Cd3^+$	0.05
As^{3+}	0.05
Cr^{3+}	1.0
Cu^{2+}	1.5
Ni^{3+}	0.1
Fe^{3+}	1.5
Mn^{2+}	1.0
Zn^{2+}	5.0
Ag^+	0.1
Ba^{3+}	2.0
Co^{2+}	2.0
Other cations	0.1
Pesticides	0.2
CN^{-1}	0.1
Industrial washing	0.5
Coli groups	4000/100 cm^3

which the measurements are carried out under an electrochemical workstation (CHI660E) using a xenon lamp.

2.4. Characterization of the Prepared Nanomaterials. The chemical structure and morphology of the prepared PANI and PANI/Ag_2O-Ag composites I and II are characterized using different analytical techniques. The X-ray diffractometer system (PX'Pert Pro, Holland) with Fourier transform infrared spectroscopy (Shimadzu FTIR-340 Jasco spectrophotometer) confirms the chemical structure and function groups while the scanning electron microscope (ZEISS Gemini Column) analyzed the morphology. The UV spectrophotometer (M160 PC) determines the optical analyses.

3. Results and Discussion

3.1. Characterization of the Prepared Nanomaterials. The chemical structures and functional groups of PANI and PANI/Ag_2O/Ag composites I and II are confirmed using the FTIR analyses as shown in Figure 2(a). Table 2 summarizes the peak positions for the function groups. For the PANI, the function groups N-H, C-H aromatic, and C-N are located at 3401, 3051, and 1105 cm^{-1}, while the C=C quinoid and benzenoid rings are located at 1467 and 1301 cm^{-1}, respectively. Moreover, the C-H in the plane and paradisubstituted rings are located at 870 and 787 cm^{-1}, respectively. After the composite formation, there are redshifts in the band positions related to N-H, C-H aromatic, C=C quinoid, C=C benzenoid, C-N, and C-H in the plane. While there are blueshifts in the band related to the paradisubstituted aromatic rings. These shifts are related to the

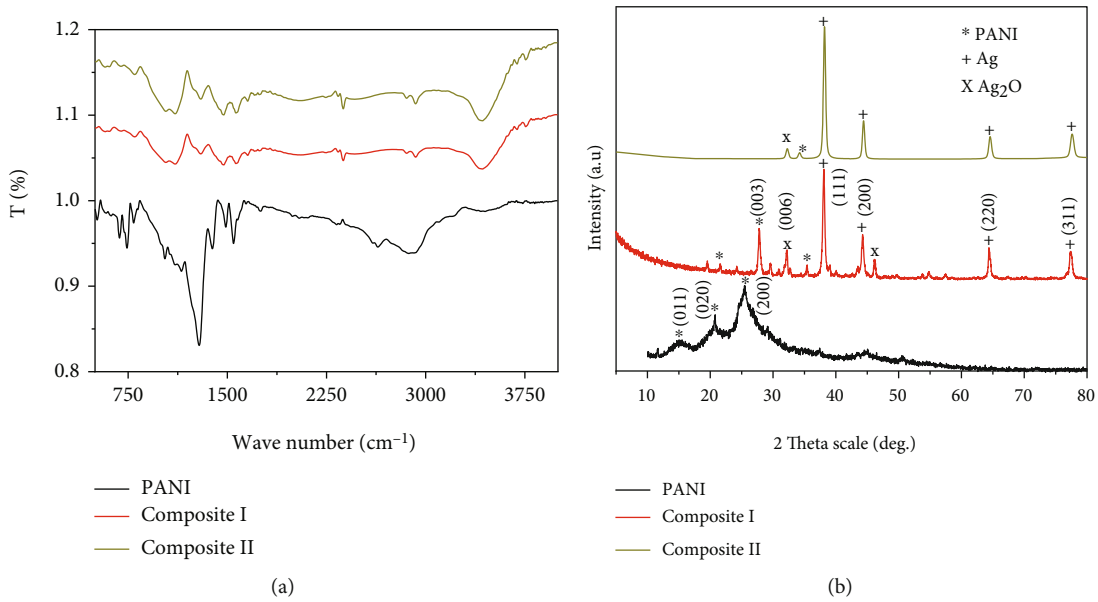

Figure 2: (a) FTIR and (b) XRD analyses of PANI and PANI/Ag_2O-Ag composites I and II.

Table 2: The FT-IR spectra of PANI and PANI/Ag_2O-Ag composites I and II.

Band position (cm^{-1})			
PANI	PANI/Ag_2O/Ag composite I	PANI/Ag_2O/Ag composite II	Assignment
3401	3449	3500	N–H group [44, 45]
3035	3038	3051	C-H aromatic ring
1467	1488	1490	C=C of the quinoid ring [44]
1301	1386	1387	C=C of benzenoid rings
1105	1153	1153	C–N
870	871	871	C–H in-plane
787	741	741	Paradisubstituted aromatic rings

effect of Ag_2O and Ag on the N atom in the nanocomposite [33].

The XRD analyses of PANI and PANI/Ag_2O-Ag composites I and II are shown in Figure 2(b). The XRD pattern of PANI (black line) shows the semicrystalline nature of the polymer related to the presence of three peaks located at 15.02, 20.78, and 25.55°. These peaks correspond to the growth directions (011), (020), and (200), respectively [34–36].

With the formation of PANI/Ag_2O-Ag composite I, there is the appearance of new peaks related to the Ag_2O at 32.3, 46.6, and 54.7° [37, 38]. Moreover, there is the appearance of new peaks related to the cubic Ag nanoparticles at 38, 44.3, 64.5, and 77.5°. These peaks have higher intensities than observed for Ag_2O in the growth directions (111, (200), (220), and (311), respectively [39].

In composite II, the peaks related to the Ag nanoparticles have almost the same positions in composite I. While the Ag_2O nanoparticles are located only at 32.13° and have the growth direction (006), the PANI indication peak is located at 34.08° through composite II, the peaks related to Ag nanoparticles increase at the same time, and there is a disappearance of peaks related to the Ag_2O in the composite.

$$D = \frac{0.9L}{\beta \cos \theta}. \quad (1)$$

Using the Scherrer equation (1) [23], the average crystalline size of Ag nanoparticles is 23 nm at 38°. This equation depends on full width at half maximum (β), the wavelength of X-ray ($L = 0.15406$ nm), and θ (half diffraction angle (degree) of peak).

The morphological analyses of the PANI and PANI/Ag_2O-Ag composites I and II are estimated by SEM analyses as shown in Figures 3(a)–3(c)). Moreover, the cross section and morphologies are confirmed by the theoretical modeling ImageJ program as shown in Figures 3(d)–3(f)). From Figure 3(a), the irregular shape of PANI appears well with porous nature and agglomerated network. This behavior is

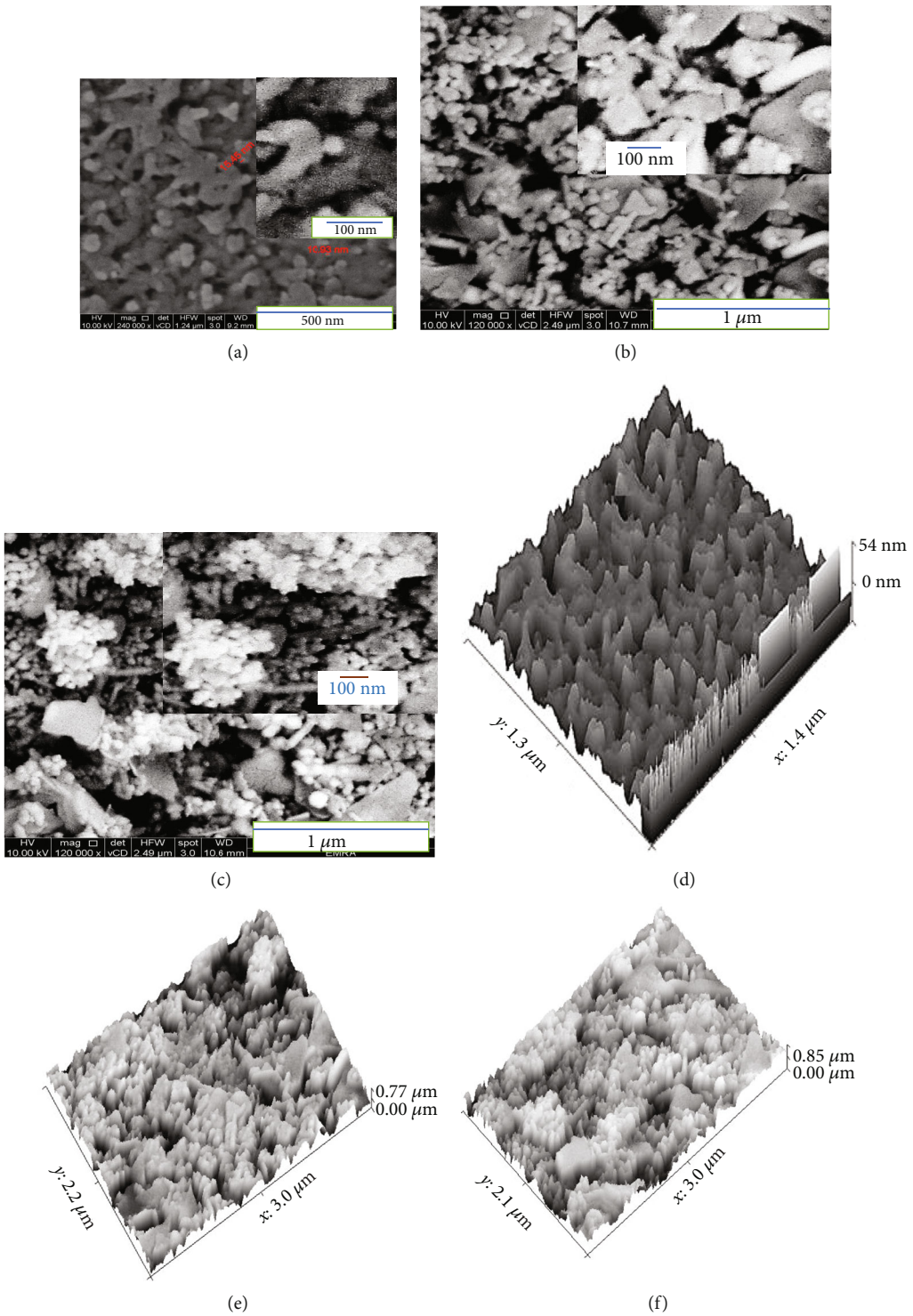

Figure 3: SEM and ImageJ modeling of (a, d) PANI, (b, e) composite I, and (c, f) composite II, respectively.

confirmed in Figure 3(d) using the modeling study. The high porosity and surface roughness are confirmed.

The morphology of composite I is shown in Figure 3(b). The Ag_2O and Ag appear as small circular nanoparticles incorporated inside the PANI particles. The surface roughness and cross section appear well using the modeling image as shown in Figure 3(e). The rough surface confirms the presence of very small particles in the composite.

The morphology of composite II is shown in Figure 3(c); from this figure, the Ag_2O and Ag increase very much in the composite; then, these small particles agglomerate on each

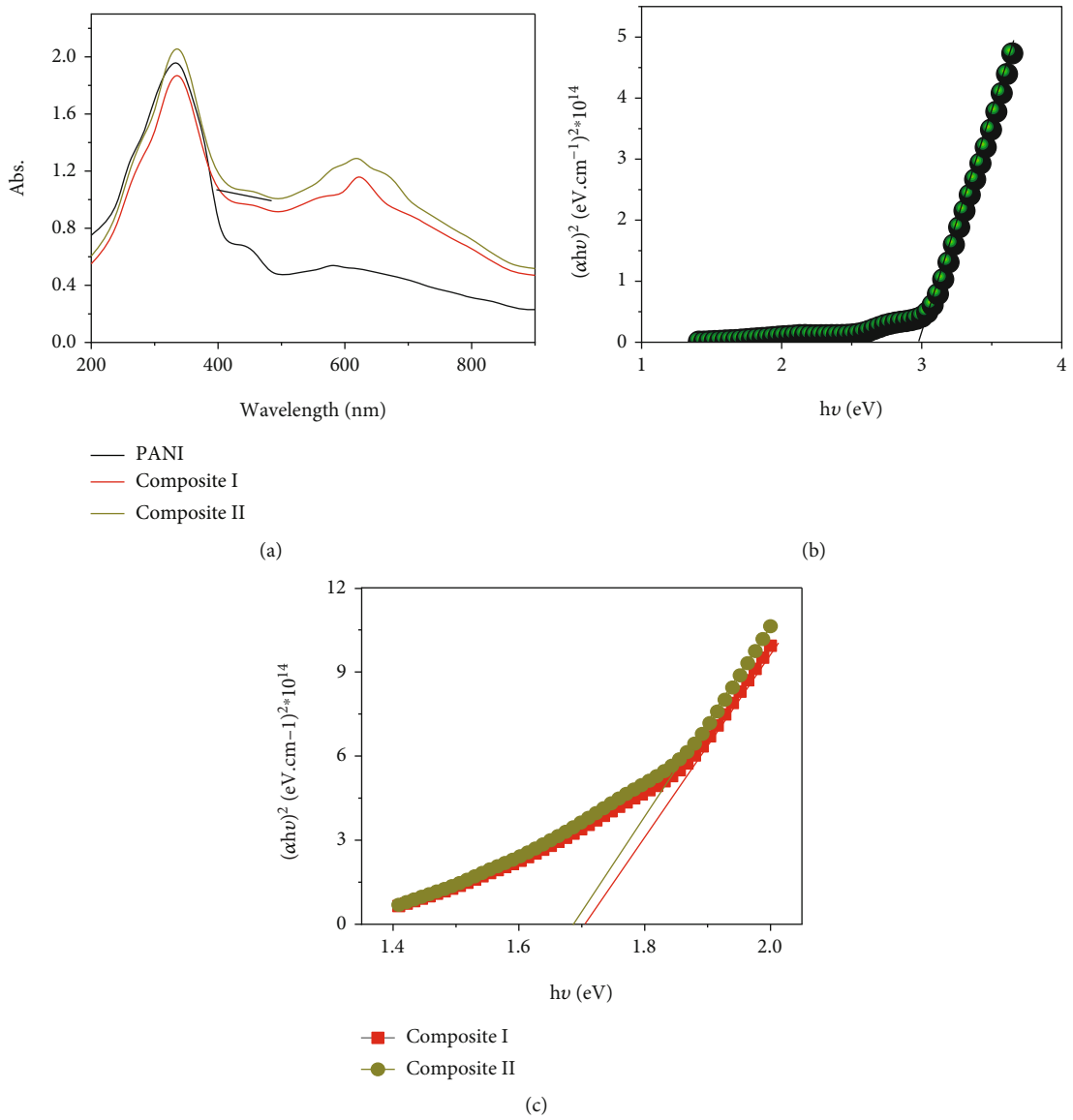

Figure 4: (a) Optical absorbance of PANI and composites I and II. Bandgap values of (b) PANI and (c) PANI/Ag_2O-Ag composites I and II.

other and form a bunch of grapes with white color. This morphology appears high clearly in Figure 3(f), in which the high roughness appears with more white color indicating the high percentage of Ag_2O and Ag in the composite.

The optical analyses of the prepared PANI and PANI/Ag_2O-Ag composites I and II are shown in Figure 4. The absorbance spectra of PANI are shown in Figure 4(a) (black line). PANI has three absorbance bands at 333, 439, and 600 nm. The absorbance peak at 333 and 439 nm in the UV and visible regions are related to the Π-$\Pi*$ transitions related to the electron transition reaction [40].

In the case of composite formation, there are more enhancements in the optical absorbance, in which the composite has the same peak at 333 nm, but there are increases in its intensity. The enhancements appear clearly in the peaks at 624 nm in the visible region. Composite II has the optimum absorbance behavior, in which it has the optimum intensity in the UV region and redshift in peaks at 624 nm. This is related to the effect of Ag_2O and Ag nanomaterials in the composite. These materials have a plasmonic response that absorbs and captures the photons; then, these photons cause electron-hole pair formation, in which the excited electron reaches the neighbor PNAI surface. Finally, these electrons do oscillation resonance motion that causes the generation of current density on the surface.

The bandgap (E_g) is calculated using Tauc's equation (equations (2) and (3)) [19, 41–43]. This bandgap depends on the absorbance (A) and absorption coefficient (α), light frequency (ν), nanomaterial density (β), Planck constant (h), and concentration of suspended material (C). Through

using the Tauc equation and Figures 4(b) and 4(c), the bandgaps of PNAI, composite I, and composite II are 3.02, 1.71, and 1.68 eV, respectively.

$$\alpha = \frac{(h\nu - Eg)1/2}{h\nu}, \tag{2}$$

$$\alpha = \frac{2.303 \times 103\, A\, \beta}{lC}. \tag{3}$$

3.2. H_2 Generation Test. The hydrogen generation under the sewage water splitting is carried out using the three-electrode cell, in which glass/PANI/Ag_2O-Ag II is the working electrode, graphite is the counter electrode, and the calomel electrode represents the reference electrode. The chemical composition of the sewage water is mentioned in Table 1.

The measurements were carried out from 100 ml of sewage water without using any additional electrolytes. The measurements were carried out under the voltage (0 to 1 V) at 25°C.

Under the applied voltage in dark and light, the current density values (J_{ph}) increase from 3.8 to 12.16 μA·cm^{-2}, respectively, as shown in Figure 5. The small J_{ph} in dark is related to the semiconductor nature of the PANI/Ag_2O-Ag. Under the light illumination, the J_{ph} value increases significantly; this is due to the high efficiency of the photocatalytic materials for the light absorbance, in which these photons do the motivation of the active sites and the generation of the electron-hole pairs under the splitting levels of the composite. The Ag nanomaterials work as plasmonic materials for the light absorbance, these materials accept the photons and generate an electric field around it, and this electron field is transferred to the neighbor semiconductor materials and causes the increase in the electron density over the semiconductor materials. The electron field spectral overlap between the oscillator frequency of PANI and Ag causes condensation of the electric field around all the composites [17]. This process causes the collections of the electrons over the composite that transfer to the neighbor sewage water for the hydrogen generation reaction and then the generation of high values of the J_{ph}.

The effect of temperature (303 to 333 K) on the produced J_{ph} values is shown in Figure 6(a). The figure confirms the increase in the J_{ph} values with temperature, in which the J_{ph} values are 0.012 and 0.032 mA cm^{-2} at 303 and 333 K, respectively. The increase in the J_{ph} values is related to the increase in the ions in solutions. This J_{ph} value represents the rate of the water splitting reaction [46]. The J_{ph} values at +1 V are represented in Figure 6(b).

The activation energy (E_a) is calculated from the Arrhenius equation (4) [47] using Figure 6(c) (black curve). The E_a value is 27.1 kJ mol^{-1}. The enthalpy ($\Delta H*$) and entropy ($\Delta S*$) values are calculated from the Eyring equation (5) [41, 43] using Figure 6(b) (red curve). From the slope of the red curve, $\Delta H*$ value is 24.5 J mol^{-1}, while the $\Delta S*$ value is 140.5 J K^{-1} mol^{-1}.

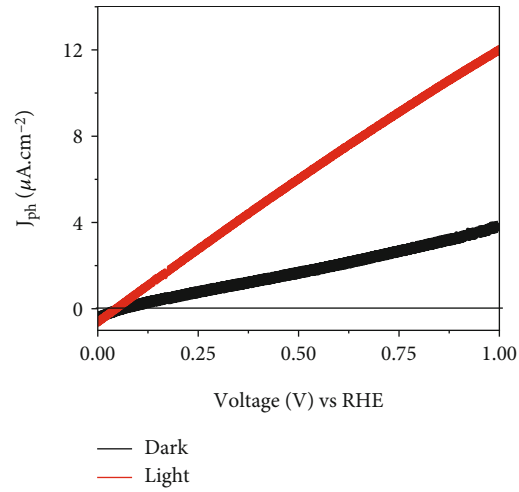

Figure 5: The produced current density under dark and light for the PANI/Ag_2O-Ag composite II at 25°C.

$$k = Ae^{-E_a/\mathrm{RT}}, \tag{4}$$

$$k = T.\frac{kB}{h}.e^{\Delta S/R}.e^{-\Delta H/\mathrm{RT}}. \tag{5}$$

The relation between the produced J_{ph} values and the light wavelengths using optical filters from 390 to 636 nm is shown in Figure 7(a). The J_{ph} value a +1 V is mentioned in Figure 7(b). From this figure, it appears that the produced J_{ph} values decrease from 6 to 4.51 μA·cm^{-2} with the increase in the light wavelengths from 390 to 508 nm and then increase again at 636 nm to reach 5.01 μA·cm^{-2}. These values are matched well with the optical analysis behavior as mentioned in Figure 4(a). The good response of the PANI/Ag_2O-Ag II is motivated by the optical plasmonic behavior of the Ag nanomaterials. This Ag atom causes the oscillation around the PANI/Ag_2O nanomaterials, in which this process activates the electrons over the nanomaterials for the additional formation of electron-hole pairs, in which the oscillation frequency of the Ag atom matched well with the oscillation of the Ag_2O and PANI. These Ag nanoparticles in the composite cause the generation of localized surface plasmonic resonance (LSPR) [48, 49]. Then, there is coupling in the electromagnetic field between the Ag and the PANI/Ag_2O nanomaterials that cause the transfer of the energy from this plasmonic material to this semiconductor materials. J_{ph} is produced as a result of the activation PANI/Ag_2O sites; this process causes the generation of electrons. This electron transfer occurs easily due to the small bandgap of the composite (as shown in the optical absorption curve (Figure 4). Under the generation of J_{ph}, the sewage water splitting and the generation are carried out. These J_{ph} values represent the rate of hydrogen generation reaction.

The relation between the time and the produced J_{ph} values is mentioned in Figure 8(a); from this figure, there is linear stability in the produced J_{ph} after a short time with a produced J_{ph} value of 2.3 μA·cm^{-2}.

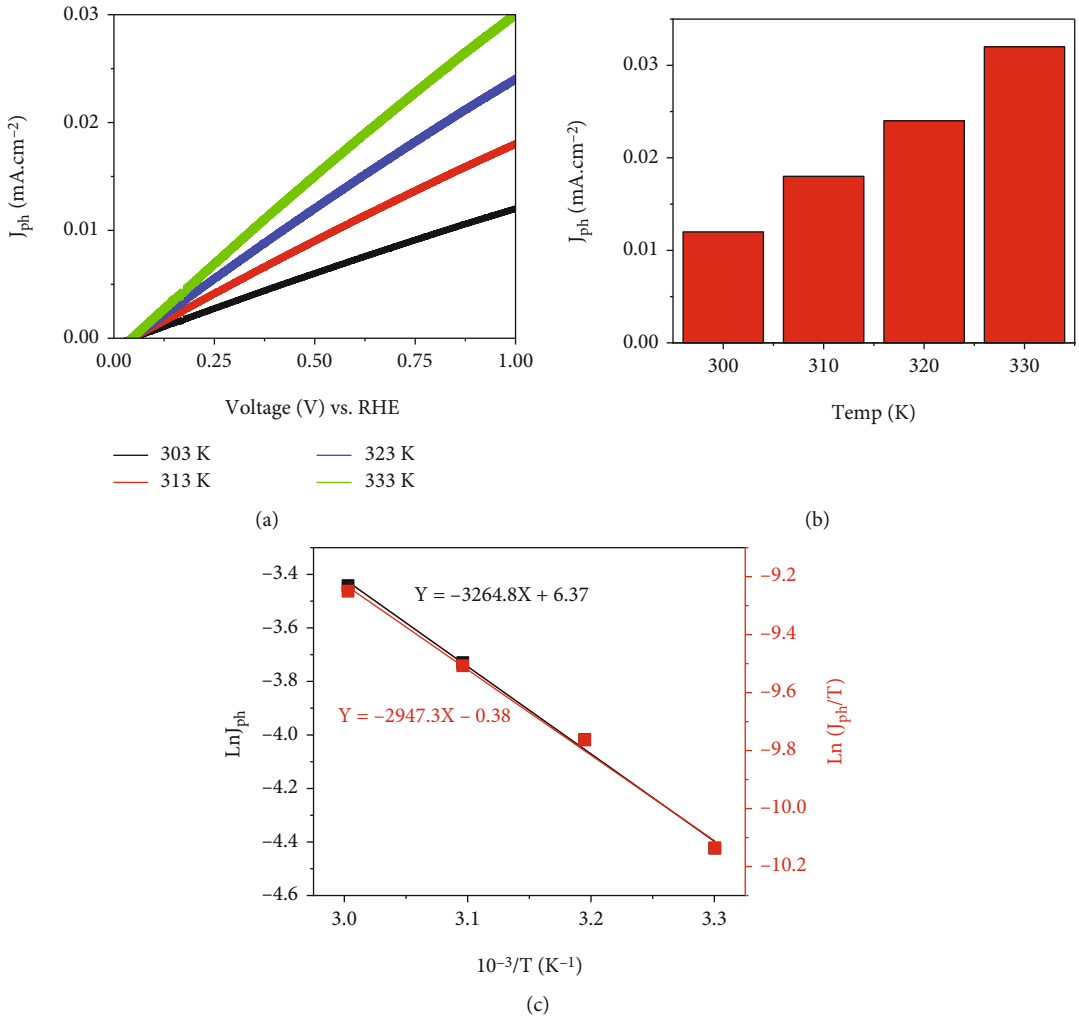

FIGURE 6: (a) The produced current density under different temperatures and (b) the produced current density at +1 V for the electrode glass/PANI/Ag_2O-Ag II. (c) The Arrhenius (black curve) and Eyring equation (red curve) relationship for calculation of the thermodynamic parameters.

Quantitatively, the generated hydrogen moles as a function of the time are determined by Faraday's law of electrolysis (6) [34] as shown in Figure 8(b).

$$H_2\text{moles} = \int_0^t J\frac{dt}{F}, \tag{6}$$

where F is the Faraday constant (the quantity of charge in Coulomb carried by one mole of electrons), J is the measured current, and t is the time. Theoretically, the calculated hydrogen moles per active area are 0.045 μmol h^{-1} cm^{-2} for the prepared electrode.

3.3. Wettability Study. Measuring the contact angle (θ) for the determination of wettability represents an important feature of the H_2 generation reaction. By increasing the wettability, the contact angle decreases, and so the high contact between the solution and the surface increases for more H_2 gas evolution. The contact angles are determined for PANI and PANI/Ag_2O/Ag composite II as shown in Figure 9. Measuring the contact angle is carried out by using Young's equation (7) [50]. The main parameters in this equation are the surface tensions for the liquid-vapor (γ_{LV}), solid-liquid (γ_{SL}), and solid vapor (γ_{SV}). The measuring process is carried out by dropping 0.1 ml of H_2O on the surface of PANI and PANI/Ag_2O/Ag composite II. As shown in Figure 9, the contact angles decrease from 92 to 37°; this confirms the enhancement in the contact between the surface and the solution. This enhancement is related to the presence of Ag_2O which is hydrophilic due to the presence of oxygen atoms [51–53].

$$\gamma LV\, Cos\,\theta = \gamma SV - \gamma SL. \tag{7}$$

Figure 9 shows the contact angle measurements; this test is carried out by dropping 0.1 ml H_2O on the surface of PMT and PMT/roll-GO, in which this angle decreases from 92 to 41°, respectively. This enhancement is related to the effect of roll-GO for the enhancement of the surface morphology and the hydrophilic nature of the composite nanomaterials [50].

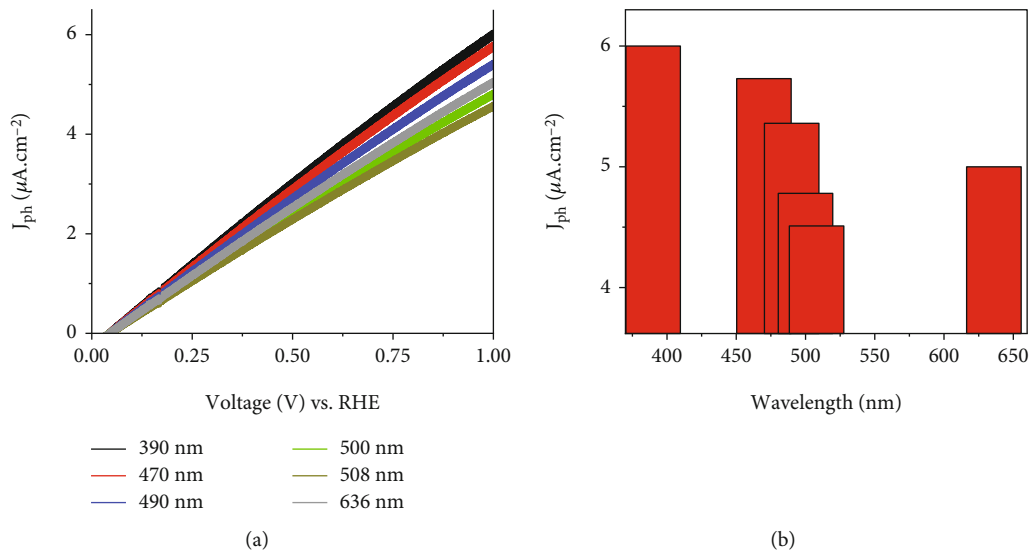

Figure 7: (a) The effect of wavelengths (390 to 636 nm) on current density for the electrode PANI/Ag_2O/Ag II and (b) the produced current density at +1 V under different wavelengths.

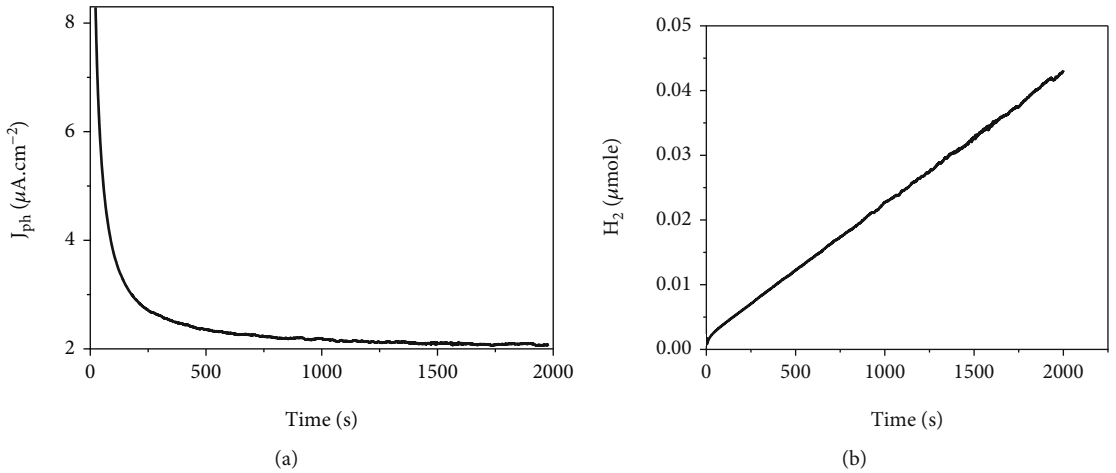

Figure 8: The relation between (a) the current density and time and (b) the produced H_2 moles and time.

Figure 9: Contact angle values for (a) PANI and (b) PANI/Ag_2O/Ag composite II.

4. Conclusions

The photopolymerization method is used for the preparation of PANI/Ag_2O/Ag composites I and II, by using 0.1 and 0.2 M $AgNO_3$, respectively. The optical analyses confirm the enhancement of the optical properties of the composites in comparison with the PANI, in which the PANI/Ag_2O/Ag composite II has the optimum optical properties with a bandgap of 1.68 eV. Glass/PANI/Ag_2O/Ag composite II is used as an electrode for hydrogen generation from sewage water without using any additional electrolyte. The measurements were carried out under dark/light and different optical

wavelengths and temperatures. At 3°C, the J_{ph} value increased from 0.003 to 0.012 mA.cm^{-2} in dark and light, respectively, and then reached 0.032 mAcm^{-2} at 60°C. Under different wavelengths, the produced J_{ph} values decrease from 6 to 4.51 μA·cm^{-2} with increase in the light wavelengths from 390 to 508 nm and then increase again at 636 nm to reach 5.01 μA·cm^{-2}. The thermodynamic parameters were calculated in which the E_a, $\Delta H*$, and $\Delta S*$ values were 27.1 kJ·mol^{-1}, 24.5 J mol^{-1}, and 140.5 J K^{-1} mol^{-1}, respectively. Soon, we will work on the synthesis of an initial industrial model of the electrode, in which the prepared electrode is a very cheap (1$ for $12 * 12$ cm^2) electrode.

Data Availability

The data that support the findings of this study are available from the corresponding author upon reasonable request.

Conflicts of Interest

The authors declare that they have no conflicts of interest.

Acknowledgments

The authors extend their appreciation to the Deanship of Scientific Research at Jouf University for funding this work through a research grant (no. DSR-2021-03-0322).

References

[1] J. Fu, Z. Fan, M. Nakabayashi et al., "Interface engineering of Ta3N5 thin film photoanode for highly efficient photoelectrochemical water splitting," *Nature Communications*, vol. 13, no. 1, pp. 1–9, 2022.

[2] H. Zhang, D. Li, W. J. Byun et al., "Gradient tantalum-doped hematite homojunction photoanode improves both photocurrents and turn-on voltage for solar water splitting," *Nature Communications*, vol. 11, no. 1, 2020.

[3] A. A. A. Abdelazeez, N. M. A. Hadia, M. Alzaid et al., "Development of CuO nanoporous material as a highly efficient optoelectronic device," *Applied Physics A*, vol. 128, no. 4, article 321, pp. 1–10, 2022.

[4] N. M. A. Hadia, A. A. A. Abdelazeez, M. Alzaid et al., "Converting sewage water into H2 fuel gas using Cu/CuO nanoporous photocatalytic electrodes," *Materials*, vol. 15, no. 4, p. 1489, 2022.

[5] H. Nishiyama, T. Yamada, M. Nakabayashi et al., "Photocatalytic solar hydrogen production from water on a 100-m^2 scale," *Nature*, vol. 598, no. 7880, pp. 304–307, 2021.

[6] M. Shaban, M. Benghanem, A. Almohammedi, and M. Rabia, "Optimization of the active layer P3HT: PCBM for organic solar cell," *Coatings*, vol. 11, no. 7, p. 863, 2021.

[7] M. Pagliaro, "Preparing for the future: solar energy and bioeconomy in the United Arab Emirates," *Energy Science & Engineering*, vol. 7, no. 5, pp. 1451–1457, 2019.

[8] T. Takata, J. Jiang, Y. Sakata et al., "Photocatalytic water splitting with a quantum efficiency of almost unity," *Nature*, vol. 581, no. 7809, pp. 411–414, 2020.

[9] Z. Kang, Y. Cheng, Z. Zheng et al., "MoS_2-based photodetectors powered by asymmetric contact structure with large work function difference," *Nano-Micro Letters*, vol. 11, no. 1, p. 34, 2019.

[10] J. H. Lee, W. W. Lee, D. W. Yang, W. J. Chang, S. S. Kwon, and W. Park, "Anomalous photovoltaic response of graphene-on-GaN Schottky photodiodes," *ACS Applied Materials and Interfaces*, vol. 10, no. 16, pp. 14170–14174, 2018.

[11] I. Ali, G. T. Imanova, X. Y. Mbianda, and O. M. L. Alharbi, "Role of the radiations in water splitting for hydrogen generation," *Sustainable Energy Technologies and Assessments*, vol. 51, article 101926, 2022.

[12] Y. Qi, J. Zhang, Y. Kong et al., "Unraveling of cocatalysts photodeposited selectively on facets of BiVO4 to boost solar water splitting," *Nature Communications*, vol. 13, no. 1, pp. 1–9, 2022.

[13] X. Li, C. H. Tung, and L. Z. Wu, "Semiconducting quantum dots for artificial photosynthesis," *Nature Reviews Chemistry*, vol. 2, no. 8, pp. 160–173, 2018.

[14] Q. Wang and K. Domen, "Particulate photocatalysts for light-driven water splitting: mechanisms, challenges, and design strategies," *Chemical Reviews*, vol. 120, no. 2, pp. 919–985, 2020.

[15] S. Cestellos-Blanco, H. Zhang, J. M. Kim, Y. X. Shen, and P. Yang, "Photosynthetic semiconductor biohybrids for solar-driven biocatalysis," *Nature Catalysis*, vol. 3, no. 3, pp. 245–255, 2020.

[16] T. Hisatomi and K. Domen, "Reaction systems for solar hydrogen production via water splitting with particulate semiconductor photocatalysts," *Nature Catalysis*, vol. 2, no. 5, pp. 387–399, 2019.

[17] H. S. H. Mohamed, M. Rabia, X. G. Zhou et al., "Phase-junction Ag/TiO_2 nanocomposite as photocathode for H_2 generation," *Journal of Materials Science & Technology*, vol. 83, pp. 179–187, 2021.

[18] M. Rabia, N. M. A. Hadia, O. M. Farid, A. A. A. Abdelazeez, S. H. Mohamed, and M. Shaban, "Poly(m-Toluidine)/rolled graphene oxide nanocomposite photocathode for hydrogen generation from wastewater," *International Journal of Energy Research*, 2022.

[19] M. Rabia, S. H. Mohamed, H. Zhao, M. Shaban, Y. Lei, and A. M. Ahmed, "TiO2/TiOxNY hollow mushrooms-like nanocomposite photoanode for hydrogen electrogeneration," *Journal of Porous Materials*, vol. 27, no. 1, pp. 133–139, 2020.

[20] K. I. Fujita, Y. Tanaka, M. Kobayashi, and R. Yamaguchi, "Homogeneous perdehydrogenation and perhydrogenation of fused bicyclic N-heterocycles catalyzed by iridium complexes bearing a functional bipyridonate ligand," *Journal of the American Chemical Society*, vol. 136, no. 13, pp. 4829–4832, 2014.

[21] R. Kato, K. Yoshimasa, T. Egashira, T. Oya, K. Oyaizu, and H. Nishide, "A ketone/alcohol polymer for cycle of electrolytic hydrogen-fixing with water and releasing under mild conditions," *Nature Communications*, vol. 7, no. 1, pp. 1–7, 2016.

[22] X. Yan, J. Biemolt, K. Zhao et al., "A membrane-free flow electrolyzer operating at high current density using earth-abundant catalysts for water splitting," *Nature Communications*, vol. 12, no. 1, pp. 1–9, 2021.

[23] M. Ahmed, M. Rabia, and M. Shaban, "The structure and photoelectrochemical activity of Cr-doped PbS thin films grown by chemical bath deposition," *Advances*, vol. 10, no. 24, pp. 14458–14470, 2020.

[24] K. Xiao, B. Tu, L. Chen et al., "Photo-driven ion transport for a photodetector based on an asymmetric carbon nitride

nanotube membrane," *Angewandte Chemie International Edition*, vol. 58, no. 36, pp. 12574–12579, 2019.

[25] K. D. Modibane, N. J. Waleng, K. E. Ramohlola et al., "Poly(3-aminobenzoic acid) decorated with cobalt zeolitic benzimidazolate framework for electrochemical production of clean hydrogen," *Polymers*, vol. 12, no. 7, pp. 1–14, 2020.

[26] E. Thimsen, F. Le Formal, M. Grätzel, and S. C. Warren, "Influence of plasmonic Au nanoparticles on the photoactivity of Fe_2O_3 electrodes for water splitting," *Nano Letters*, vol. 11, no. 1, pp. 35–43, 2011.

[27] S. Ghosh, N. A. Kouamé, L. Ramos et al., "Conducting polymer nanostructures for photocatalysis under visible light," *Nature Materials*, vol. 14, no. 5, pp. 505–511, 2015.

[28] Z. Yin and Q. Zheng, "Controlled synthesis and energy applications of one-dimensional conducting polymer nanostructures: an overview," *Advanced Energy Materials*, vol. 2, no. 2, pp. 179–218, 2012.

[29] G. Liu, S. K. Karuturi, H. Chen et al., "Enhancement of the photoelectrochemical water splitting by perovskite $BiFeO_3$ via interfacial engineering," *Solar Energy*, vol. 202, pp. 198–203, 2020.

[30] Z. Wang, D. Cao, L. Wen et al., "Manipulation of charge transfer and transport in plasmonic-ferroelectric hybrids for photoelectrochemical applications," *Nature Communications*, vol. 7, no. 1, pp. 1–8, 2016.

[31] E. Freeman, S. Kumar, S. R. Thomas, H. Pickering, D. J. Fermin, and S. Eslava, "PrFeO3 photocathodes prepared through spray pyrolysis," *ChemElectroChem*, vol. 7, no. 6, pp. 1365–1372, 2020.

[32] B. D. Sherman, D. L. Ashford, A. M. Lapides, M. V. Sheridan, K. R. Wee, and T. J. Meyer, "Light-driven water splitting with a molecular electroassembly-based core/shell photoanode," *Journal of Physical Chemistry Letters*, vol. 6, no. 16, pp. 3213–3217, 2015.

[33] E.-S. M. Sayyah, M. Shaban, and M. Rabia, "A sensor of m-cresol nanopolymer/Pt-electrode film for detection of lead ions by potentiometric methods," *Advances in Polymer Technology*, vol. 37, no. 5, 2018.

[34] M. Rabia, H. S. H. Mohamed, M. Shaban, and S. Taha, "Preparation of polyaniline/PbS core-shell nano/microcomposite and its application for photocatalytic H_2 electrogeneration from H_2O," *Scientific Reports*, vol. 8, no. 1, 2018.

[35] M. Rabia, M. Shaban, A. Adel, and A. A. Abdel-Khaliek, "Effect of plasmonic au nanoparticles on the photoactivity of polyaniline/indium tin oxide electrodes for water splitting," *Environmental Progress & Sustainable Energy*, vol. 38, no. 5, p. 13171, 2019.

[36] M. Shaban, M. Rabia, A. M. A. El-Sayed, A. Ahmed, and S. Sayed, "Photocatalytic properties of PbS/graphene oxide/polyaniline electrode for hydrogen generation," *Scientific Reports*, vol. 7, no. 1, pp. 14100–14113, 2017.

[37] J. Wei, Y. Lei, H. Jia, J. Cheng, H. Hou, and Z. Zheng, "Controlled in situ fabrication of Ag2O/AgO thin films by a dry chemical route at room temperature for hybrid solar cells," *Dalton Transactions*, vol. 43, no. 29, pp. 11333–11338, 2014.

[38] O. Pawar, N. Deshpande, S. Dagade, S. Waghmode, and P. Nigam Joshi, "Green synthesis of silver nanoparticles from purple acid phosphatase apoenzyme isolated from a new source Limonia acidissima," *Journal of Experimental Nanoscience*, vol. 11, no. 1, pp. 28–37, 2016.

[39] M. M. Abdelhamied, A. Atta, A. M. Abdelreheem, A. T. M. Farag, and M. M. El Okr, "Synthesis and optical properties of PVA/PANI/Ag nanocomposite films," *Journal of Materials Science: Materials in Electronics*, vol. 31, pp. 22629–22641, 2020.

[40] A. A. A. Abdelazeez, G. A. El-Fatah, M. Shaban, A. M. Ahmed, and M. Rabia, "ITO/poly-3-methylaniline/Au electrode for electrochemical water splitting and dye removal," *ECS Journal of Solid State Science and Technology*, vol. 10, no. 12, article 123009, 2021.

[41] A. Almohammedi, M. Shaban, H. Mostafa, and M. Rabia, "Nanoporous TiN/TiO2/alumina membrane for photoelectrochemical hydrogen production from sewage water," *Nanomaterials*, vol. 11, p. 2617, 2021.

[42] A. M. Elsayed, M. Rabia, M. Shaban, A. H. Aly, and A. M. Ahmed, "Preparation of hexagonal nanoporous Al_2O_3/TiO_2/TiN as a novel photodetector with high efficiency," *Scientific Reports*, vol. 11, no. 1, p. 17572, 2021.

[43] S. H. Mohamed, H. Zhao, H. Romanus et al., "Optical, water splitting and wettability of titanium nitride/titanium oxynitride bilayer films for hydrogen generation and solar cells applications," *Materials Science in Semiconductor Processing*, vol. 105, article 104704, 2020.

[44] D. Kowalczuk and M. Pitucha, "Application of FTIR method for the assessment of immobilization of active substances in the matrix of biomedical materials," *Materials*, vol. 12, 2019.

[45] F. Weli Asker, Z. Z. Mahamad, A. G. Eliwei, and O. A. Nief, "Synthesis and characterization of some sulfonamide dervatives," *International Journal of Applied Chemistry*, vol. 13, pp. 169–177, 2017.

[46] F. Mohamed, M. Rabia, and M. Shaban, "Synthesis and characterization of biogenic iron oxides of different nanomorphologies from pomegranate peels for efficient solar hydrogen production," *Journal of Materials Research and Technology*, vol. 9, no. 3, pp. 4255–4271, 2020.

[47] M. Rabia, M. Shaban, B. M. Jibali, and A. A. Abdelkhaliek, "Effect of annealing temperature on the photoactivity of ITO/VO 2 (M)/Au film electrodes for water splitting," *Journal of Nanoscience and Nanotechnology*, vol. 20, no. 7, pp. 4120–4130, 2020.

[48] S. Feng and W. Ji, "Advanced nanoporous anodic alumina-based optical sensors for biomedical applications," *Frontiers in Nanotechnology*, vol. 3, p. 36, 2021.

[49] C. Langhammer, M. Schwind, B. Kasemo, and I. Zorić, "Localized surface plasmon resonances in aluminum nanodisks," *Nano Letters*, vol. 8, no. 5, pp. 1461–1471, 2008.

[50] M. S. S. Fadel, M. Rabia, S. Ezzat, N. Mansour, E. Saeed, and S. M. Sayyah, "Effect of annealing temperature on VO2(M)/ITO film nanomaterials for thermochromic smart windows application and study its contact angle," vol. 12, p. 16009, 2018.

[51] G. F. Teixeira, E. Silva Junior, R. Vilela, M. A. Zaghete, and F. Colmati, "Perovskite structure associated with precious metals: influence on heterogenous catalytic process," *Catalysts*, vol. 9, no. 9, p. 721, 2019.

[52] M. Mishra and D. M. Chun, "α-Fe_2O_3 as a photocatalytic material: a review," *Applied Catalysis A: General*, vol. 498, pp. 126–141, 2015.

[53] C. Acar, I. Dincer, and G. F. Naterer, "Review of photocatalytic water-splitting methods for sustainable hydrogen production," *International Journal of Energy Research*, vol. 40, no. 11, pp. 1449–1473, 2016.